Available online at www.sciencedirect.com

ScienceDirect

Advances in Space Research 69 (2022) 856–868

ADVANCES IN SPACE RESEARCH (a COSPAR publication)

www.elsevier.com/locate/asr

Wake formation behind Langmuir probes in ionospheric plasmas

Chun-Sung Jao [a,b], Sigvald Marholm [a,c], Andres Spicher [a,d], Wojciech J. Miloch [a]

[a] Department of Physics, University of Oslo, Oslo, Norway
[b] Department of Space Science and Engineering, National Central University, Taoyuan City, Taiwan
[c] Department of Computational Materials Processing, Institute for Energy Technology, Kjeller, Norway
[d] Department of Physics and Technology, The Arctic University of Norway, Tromsø, Norway

Received 21 January 2021; received in revised form 7 November 2021; accepted 13 November 2021
Available online 20 November 2021

Abstract

This paper presents a simulation study of the wake formation behind a Langmuir probe thinner than the Debye Length in the space environments such as the ionosphere's F region. We find that the wakes formed in plasma density and electric potential behind the positively biased probe can extend up to 15 Debye lengths in the subsonic plasma flow. Higher electric bias and flow velocity can further enhance the plasma wake perturbations. With an external magnetic field parallel to the object's axis, the plasma wake becomes asymmetric and more extensive than for the unmagnetized case. The wing structures in the electron and ion densities are also observed along the background magnetic field in the case of subsonic plasma flow. The quantitative results in this paper may provide a practical reference for data processing and the future design of the Langmuir probe instrument flying in the F region on such as sounding rockets and low Earth orbit (LEO) satellite missions. In particular, since the Langmuir probe instrument may comprise two or more biased Debye-scale Langmuir probes, the plasma wake formed behind a single probe may influence the measurements from other instruments onboard.

Keywords: Wake formation; Langmuir probes; Ionospheric plasma; Particle-in-cell simulation

1. Introduction

Space plasma research has utilized ground-based observation and in-situ measurements for the exploration of the Sun-Earth environment. For the in-situ measurements, instrument-carrying rockets and satellites are designed to conduct experiments along the spacecraft's trajectory. Among these in-situ missions, it is widespread to employ Langmuir probes for the density and temperature measurements (e.g. Jacobsen et al., 2010; Fowler et al., 2015; Shebanits et al., 2020; Chernyshov et al., 2020). As a biased conductor, the Langmuir probe collects an amount of charged particles that depends on the voltage and result into the so-called current–voltage characteristic. The characteristic can be derived analytically from the Orbital Motion-Limited (OML) theory (Mott-Smith and Langmuir, 1926).

Operating classical Langmuir probes requires sweeping the bias voltages from the ion saturation region to the electron saturation region. Based on the shape of the obtained current–voltage characteristics (slopes and intersections, for example), we can infer physical parameters such as ion density, electron density, and electron temperature (Mott-Smith and Langmuir, 1926). The so-called multi-needle Langmuir probe (m-NLP) instrument consists of two or more fixed-bias cylindrical Langmuir probes (Bekkeng et al., 2010; Jacobsen et al., 2010) that are small compared to the Debye length. In particular, based on the OML theory, the current I_p collected by small fixed-bias cylindrical probes can be written as

E-mail addresses: csjao@jupiter.ss.ncu.edu.tw (C.-S. Jao), sigvald.marholm@fys.uio.no (S. Marholm), andres.spicher@fys.uio.no (A. Spicher), w.j.miloch@fys.uio.no (W.J. Miloch)

https://doi.org/10.1016/j.asr.2021.11.012
0273-1177/

$$I_P^2 = \left(\frac{\sqrt{2}n_e eA}{\pi\sqrt{m_e}}\right)^2 [kT_e + e(V_0 + V_{0p})], \quad (1)$$

where V_{0p} is the fixed bias with respect to the spacecraft, and V_0 is the unknown floating potential with respect to the ambient plasma (Mott-Smith and Langmuir, 1926; Hoang et al., 2018). A is the surface area of the probes. With the collected current I_{P1} and I_{P2} by the probes with different biases V_{01} and V_{02}, respectively, we can eliminate the unknown V_0 and electron temperature T_e and infer the electron density by

$$n_e^2 = \frac{\pi^2 m_e}{2A^2 e^3}\left(\frac{I_{P2}^2 - I_{P1}^2}{V_{02} - V_{01}}\right). \quad (2)$$

The advantage of the m-NLP system is that it can provide electron density measurements with a high sampling rate ($\sim$ kHz) since it does not require sweeping over different voltages (Bekkeng et al., 2010; Jacobsen et al., 2010). The m-NLP instrument thus becomes an appropriate option to acquire high-resolution electron density data (Jacobsen et al., 2010). This is useful for instance for the Investigation of Cusp Irregularities (ICI) missions, consisting of a series of sounding rocket experiments designed to study the irregularities and turbulence in the high latitude F region ionosphere (Moen et al., 2013). With the same consideration, the m-NLP system was also included on other sounding rockets such as ECOMA (e.g. Bekkeng et al., 2013), ICI-3 (e.g. Spicher et al., 2016), MAXIDUSTY (Antonsen et al., 2019), the ones from the Grand Challenge Initiative CUSP (Moen et al., 2018), and on satellites such as NorSat-1 (Hoang et al., 2018) or cubesats (Hoang et al., 2019).

However, a traveling object can disturb the local plasma environment. The interaction between the moving object and its surrounding plasma can lead to a plasma wake in the downstream region (Al'pert et al., 1966; Gurevich et al., 1969; Liu, 1969; Whipple, 1981; Samir et al., 1983; Wang and Hastings, 1992; Hutchinson, 2012; Deca et al., 2013; Toledo-Redondo et al., 2019). The wake can potentially lead to measurement errors (Rylina et al., 2002; Roussel and Berthelier, 2004; Engwall et al., 2006; Eriksson et al., 2006; Miyake et al., 2013). It is rational to expect that the main rocket or spacecraft body will cause the primary disturbance (Hastings, 1995; Endo et al., 2015). For instance, in such ICI missions, which employ sounding rockets for the in-situ measurement in the F region of Earth's ionosphere, spacecraft (here means the main rocket body) charging and wake formation issues thus become one primary concern for the experiments. The past studies have shown that the interaction between the main rocket body and ionospheric plasma will reach equilibrium after several plasma periods (Darian et al., 2017). The rocket will typically become negatively charged (~ -1 V in the equilibrium), and the plasma wakes behind the rocket can extend to 30 Debye lengths (20–30 cm in the ionospheric F-region plasma) (Darian et al., 2017). Meanwhile, by considering the wake potential behind the spinning rocket, the inferred wake modulation filter can significantly improve data quality (Paulsson et al., 2018). Besides the main rocket body, since the Langmuir probes are often mounted on a boom, it is also essential to consider the charging effects and the plasma disturbance in the vicinity of the boom (Paulsson et al., 2019). Note that, even though it is possible to analyze these plasma–object interaction problems theoretically under a simplified and idealized condition, numerical simulations can provide new insight with fewer assumptions and flexible set up (Marholm et al., 2019; Marholm and Marchand, 2020).

To be able to correctly interpret in-situ data, it is essential to understand the impact of plasma-probe interactions on the measurements. This comprises the effect of the large-scale objects above-mentioned, and the one associated smaller objects such as the Langmuir probes themselves. In the present paper, we investigate the importance of the latter, with particular emphasis on wake formation behind single small cylindrical Langmuir probes in flowing ionospheric plasmas. We will also discuss how far such probes should be placed from each other to avoid plasma measurement errors. Referring to the Debye length in the Earth's ionosphere, since the Langmuir probes' radius has to be much smaller than the Debye shielding distance (Jacobsen et al., 2010), the Langmuir probe's radius in the m-NLP instrument is generally smaller than 1 mm. It is worth noting that, in contrast with the main rocket body and the boom traveling with a floating potential, the Langmuir probes here will have a fixed positive bias of a few volts with respect to the rocket (Darian et al., 2017; Paulsson et al., 2018; Paulsson et al., 2019). However, as mentioned above, with a sounding rocket traveling in the ionospheric plasma, we can expect a floating potential ~ -1 V in the equilibrium (Darian et al., 2017).

The organization of this paper is as follows. In Section 2, we will first introduce the simulation setup and the parameters used in different cases. We will show the simulation results in Section 3, and the discussion and the comparisons with other studies are given in Section 4. Section 5 is the Summary.

2. Simulation setup

For the simulations in this paper, we employ a three-dimensional unstructured Particle-in-cell code, PTetra, which can simulate the time-dependent interaction of satellites with space plasmas (Marchand, 2012; Marchand and Resendiz Lira, 2017). As shown in Fig. 1, we construct a simulation domain of tetrahedral cells in a lantern shape lying along the x-axis. The largest cross-section along the x-axis is on x = 0 with $H_l = 20$ cm and $W_l = 12$ cm. The cross section is constructed by two symmetric arches with the center of a circle on $(0, \pm(H_l^2 + W_l^2)/W_l - W_l, 0)$, respectively. The section's area is decreasing along both $\pm\hat{x}$ directions, and the smallest sections with $H_s = 8$ cm

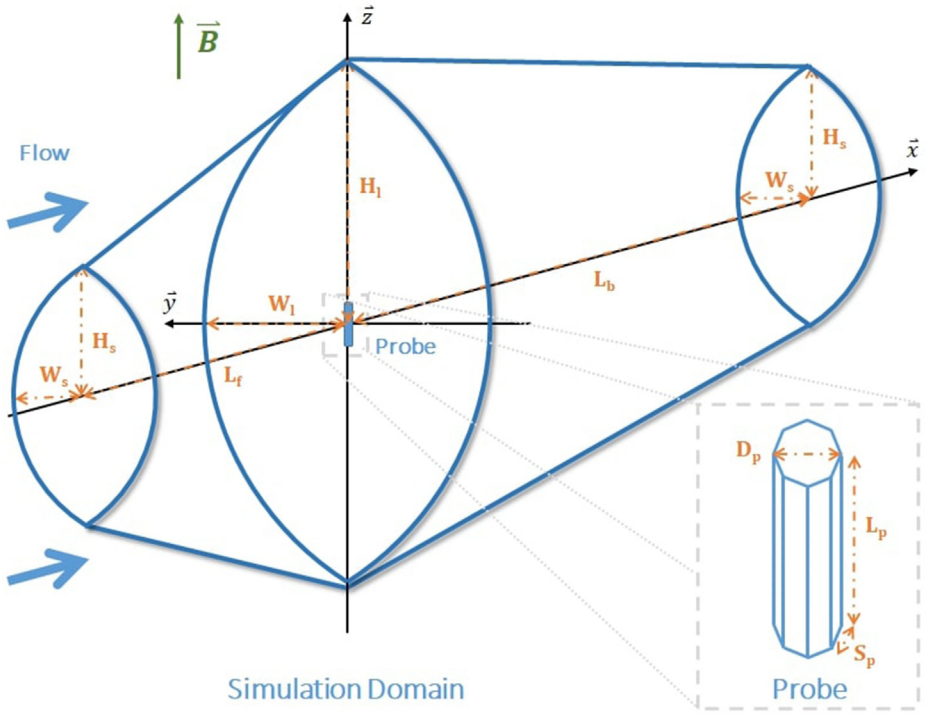

Fig. 1. The sketch of the simulation domain.

and $W_s = 4$ cm are in the front and back of the simulation domain, x $= -L_f$ and x $= L_b$, where $L_f = 12$ cm and $L_b = 40$ cm.

Focusing on the interaction between a single Langmuir probe and its surrounding plasma, we set a Langmuir probe as an octagonal prism standing along the z-axis with its center on the origin of coordinate. As also shown in Fig. 1, L_p and D_P are the length and the diameter of the Langmuir probe, respectively. The bias on the Langmuir probe ϕ is a variable in the presented cases. Note that here the zero potential is set on the boundary of the simulation domain. In a realistic situation, the fixed positive bias on the Langmuir probes is with respect to the rocket, which means that the probe potential will vary with respect to the plasma according to the rocket's floating potential. As mentioned above, the interaction between the main rocket body and the F-region ionospheric plasma will reach equilibrium in a few ion plasma periods and reach a final floating potential ~ -1 V, which can also be related to the plasma temperature (Darian et al., 2017). Here, however, we only simulate a probe with a fixed voltage with respect to the plasma in order not to simulate the entire spacecraft. It is also worth mentioning the finite-length effects on cylindrical Langmuir probes (Marholm and Marchand, 2020). The fact that both ends of the simulated probe are free instead of one being mounted on a spacecraft will inevitably lead to an enhanced current collection. However, in this paper, our concern is the wake directly behind the probe and not the collected current. Setting up the whole m-NLP instrument will cause prohibitive computational cost due to the large scale differences between the probe radius and spacecraft dimensions. But, to some extent, our simulation model corresponds to the real situation where the probes are attached to the boom to avoid interference from the spacecraft sheath and there is a cylindrical segment (the guard) between the boom and the probe. Since the plasma wake caused by the boom is generally within a few Debye lengths (Paulsson et al., 2019), it is reasonably assumed that the boom sheath does not interfere with the probe measurement.

To mimic the ionospheric environment in the simulation system, as shown in Table 1, the background plasma with electrons and ions is set with the number density $n_0 = n_i = n_e = 2 \times 10^{11}$ m^3 and the temperature $T = T_i = T_e = 2000$ K $(1.72 \times 10^{-1}$ eV). Thus the Debye

Table 1
Plasma parameters in the simulation system.

Parameter		Value
Plasma density	n_0	2×10^{11} m^{-3}
Electron temperature	T_e	2000 K
Electron plasma period	$2\pi/\omega_{pe}$	0.25 μs
Debye Length	λ_D	6.91 mm
Mass ratio	m_i/m_e	1836
Ion temperature	T_i	2000 K
Ion plasma period	$2\pi/\omega_{pi}$	10.68 μs
Sound Speed	c_s	5744 m/s
Magnetic field [a]	B_0	50 μT
Electron gyro-period [a]	$2\pi/\omega_{ce}$	0.72 μs
Electron gyroradius [a]	v_{the}/ω_{ce}	1.98 cm
Ion gyro-period [a]	$2\pi/\omega_{ci}$	1.31 ms
Ion gyroradius [a]	v_{thi}/ω_{ci}	84.9 cm

[a] If the magnetic field is applied in the simulation system.

length in the system is $\lambda_D = 6.91$ mm. Note that with the temperatures specified in Table 1 for applications to the Earth's F-region ionosphere, the sound speed is $c_s = 1436$ m/s based on the definition $c_s = \sqrt{(k_b T_i + k_b T_e)/m_i}$, where k_b is the Boltzmann constant and the ion mass m_i is that of oxygen ions. In addition the neutral particles or fluids are not included in the present study considering that the collisions between ions or electrons and neutrals are relatively weak in the upper ionosphere. In particular, the electron-neutral and ion-neutral collision frequencies are ~1000 Hz and <100 Hz, respectively, at the altitude above 200 km in the Earth's ionosphere (Kelley, 1989; Schunk and Nagy, 2009). We take the sounding rocket and the Langmuir probe's moving frame as the rest frame in our simulation system and the plasma flow is along the x-axis. Note that the speed of the sounding rocket is generally around 1 to 1.5 km/s, which is mainly in the subsonic regime. However, with a plasma flow of with opposite direction of 500 m/s to the sounding rocket, a relative flow speed can become supersonic. Thus we will also include the supersonic cases, which can be applied for the employment of the m-NLP instrument on the low Earth orbit satellites such as NorSat-1 and QB50. (Hoang et al., 2018, 2019)

In the following section, we will first present the simulation results of nine typical cases under different circumstances. Table 2 lists the varied simulation parameters for these cases. Note that here, we first adopt protons as the ion species in consideration of computing resources. When the mass ratio is set to be $m_i/m_e = 1836$, the sound speed increases to $c_s = 5744$ m/s, and the drift velocity is increased proportionally to retain the correct Mach number when employing protons instead of oxygen ions, in the simulations. The effect of the mass ratio reduction will be presented after the discussion of these typical cases. Here we will first discuss the cases with a Langmuir probe with a voltage self-consistently determined from the charged particles hitting on it (Case A and Case B for the unmagnetized and magnetized systems, respectively). In the magnetized system (Cases B and D to I), we set a background magnetic field $B_0 = 50\,\mu$T parallel to the probe's axis. We further adopt a fixed bias 3 V or 6 V in other cases (Cases C to I). Since the plasma wake behind the object is more significant in the supersonic flow, in most of the cases (Cases A to E, H, and I), we set up a supersonic plasma flow with the Mach number $M = u/c_s \sim 1.33$ ($u = 7660$ m/s, which is also the orbital speed of the International Space Station). For comparisons, we also use $M = 0.66$ and $M = 1$ in Cases F and G, respectively. The octagon's diameter D_P is another variable, ranging from 1 mm to 4 mm, to be studied in Cases D, H, and I. After discussing these typical circumstances (Cases A to I), we will present a comprehensive survey with varying Mach numbers and biases for the magnetized system (referring to Cases D to G) in the end of Section 3.

Table 2
Simulation parameters that are varied for each study case.

Case	M	B_0 (μT)	ϕ (V)	D_P (mm)
A	1.33	0	no	4
B	1.33	50	no	4
C	1.33	0	3	4
D	1.33	50	3	4
E	1.33	50	6	4
F	0.67	50	3	4
G	1.00	50	3	4
H	1.33	50	3	2
I	1.33	50	3	1

To reach equilibrium, we let the simulation run until $t = 2 \times 10^{-4}$ s, that is, for about 20 ion plasma periods. The mesh resolution at the outer boundary is the Debye length in the simulation system. Since the probe's radius is smaller than the Debye length in the simulation system, the mesh resolution at the inner boundary will also vary with the size of Langmuir probes as $\Delta x_{in} = 0.5\ S_p$, where S_p is the side length of the octagon. In the simulation domain, the total number of cells is also varied from ~270000 to 330000 with the varied Δx_{in}, and we employ fifty million superparticles (the number may fluctuate a bit throughout the simulation) for each species in all presented cases.

The purpose of this paper is to study how far such probes should be placed from each other to avoid plasma measurement errors. We will focus on the density perturbation directly and the changes in the density will affect the currents collected (as shown in Eq. 1). In all figures, the physical quantities shown are the average values in the final ion plasma period. We have also subtracted the convective electric field ($-\vec{u} \times \vec{B}_0$) in the plots of electric potential profiles for the magnetized cases.

3. Simulation results

We will first present the cases with a Langmuir probe with no fixed bias (Case A and Case B). In these cases, the electric potential of the probe will float based on the current it collects. Fig. 2(a) and (b) shows the 2D electric potential profiles for Case A and Case B, respectively. Fig. 3(a) and (b) shows the 2D ion density profiles for Case A and Case B, respectively. Fig. 4(a) and (b) shows the 2D electron density profiles for Case A and Case B, respectively. On the x-y plane (top view, $x = 0$) and x-z plane (side view, $y = 0$) in these figures, the black shadows at the origin of the coordinate system is the Langmuir probe. As indicated, compared with other no-bias objects such as the main rocket body and boom (Darian et al., 2017; Paulsson et al., 2018), the lack of geometric wake is reasonable due to its relatively tiny size. Besides, in both cases, since the electrons are more mobile than ions, the electric potential on the probe becomes negative based on the current it collects. When the charging process reaches steady-state, the probe's potential is lower than −0.36 V (red dashed contour) and reaches ~ −0.5 V in equilibrium. It

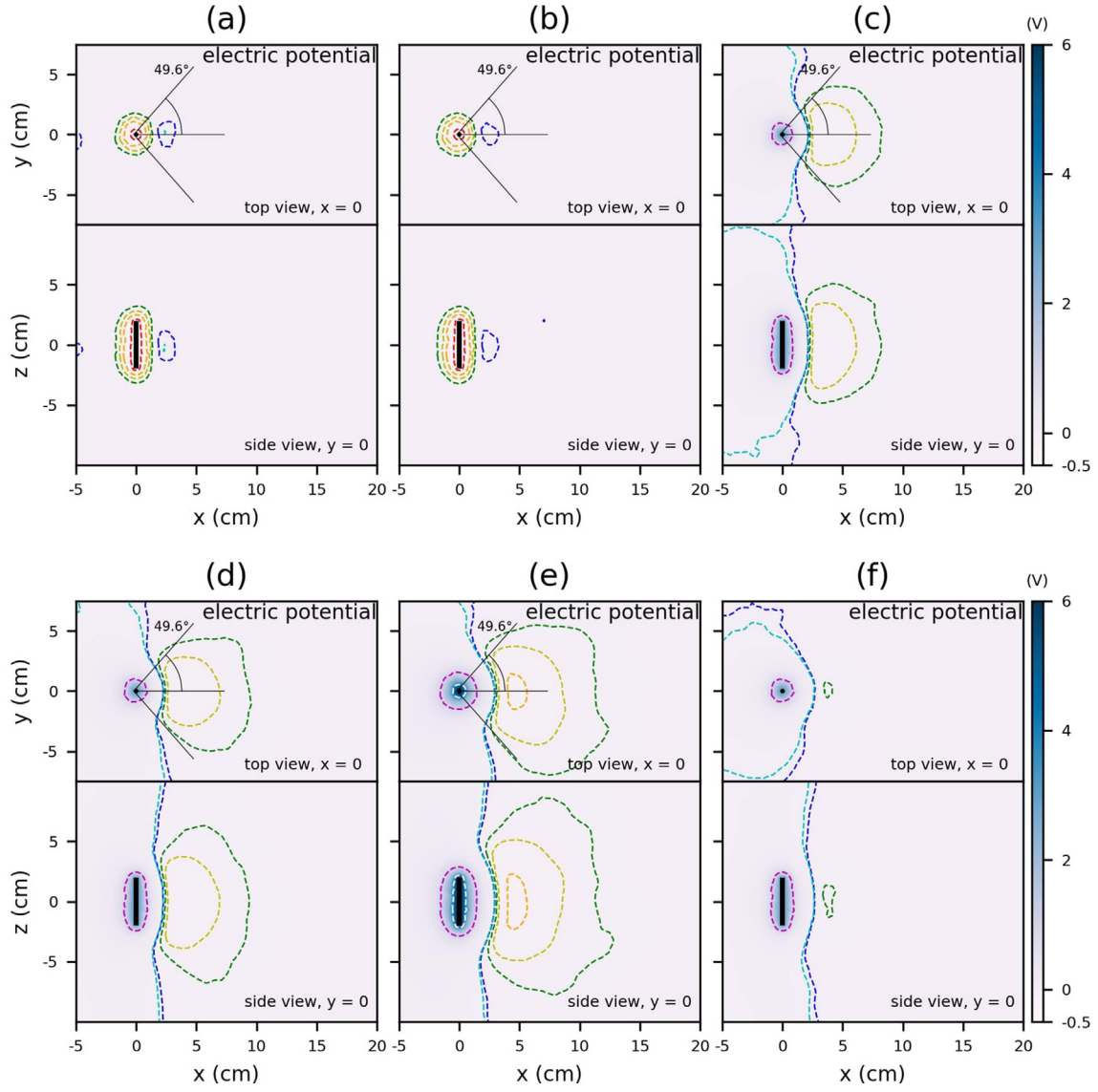

Fig. 2. The top-view (x = 0) and side-view slices (y = 0) of electric potential profiles for (a) Case A (no bias, unmagnetized, supersonic), (b) Case B (no bias, magnetized, supersonic), (c) Case C (3 V, unmagnetized, supersonic), (d) Case D (3 V, magnetized, supersonic), (e) Case E (6 V, magnetized, supersonic), and (f) Case F (3 V, magnetized, subsonic). The dashed curves show the potential contours of −0.36 V (red curves), −0.12 V (orange curves), −0.06 V (yellow curves), −0.03 V (green curves), 0.006 V (blue curves), 0.012 V (cyan curves), 1.0 V (magenta curves), and 4.0 V (white curves). The black shadows at the origin of the coordinate system is the Langmuir probe. For the supersonic cases (Case A to Case E), the Mach cone is plotted with the black line with the half angle $\theta = \arcsin(1/M)$. (For interpretation of the references to color in this figure legend, the reader is referred to the web version of this article.)

is in good agreement with the theoretical prediction that the expecting floating potential is $-2.5\ kT_e/e$ in the hydrogen plasma (Howard, 1961), while the plasma temperature is $\sim 1.72 \times 10^{-1}$ eV). As a result, as also indicated in Fig. 6 (blue curves, Case B), a negatively charged object in the plasma will attract ions and repel electrons in the object's vicinity. Thus, in the ion density, we find the ion-focusing area with a maximum density of $2.4 \times 10^{11}\ m^{-3}$ (cyan dashed contour in both Fig. 3(a) and (b)) behind the Langmuir probe (Miloch et al., 2008), which accompanies a positive potential wake (blue and cyan dashed contours on Fig. 2(a) and (b)). The length on the ion wake and the size of the focusing area are $\sim$ 1 cm ($\sim 1.4\lambda_D$) and 4 cm ($\sim 5.8\lambda_D$), respectively. Note that the ion gyroradius (84.9 cm) is relatively large in the magnetized system. Thus, in both electric potential and density profiles, we do not observe any obvious difference caused by the background magnetic field's presence in Case B compared with Case A since the ion dynamics mainly determine the ion focusing. Only the potential wake is more pronounced in the unmagnetized case (Case A, $>$ 0.012eV, cyan dashed contour) than in the magnetized case (Case B). Note that, as indicated in Fig. 5, the history of the current collected by probes, the present cases have reached steady state within 1 ion plasma periods ($t \sim 1 \times 10^{-5}$ s), and the net collected current is zero in the equilibrium.

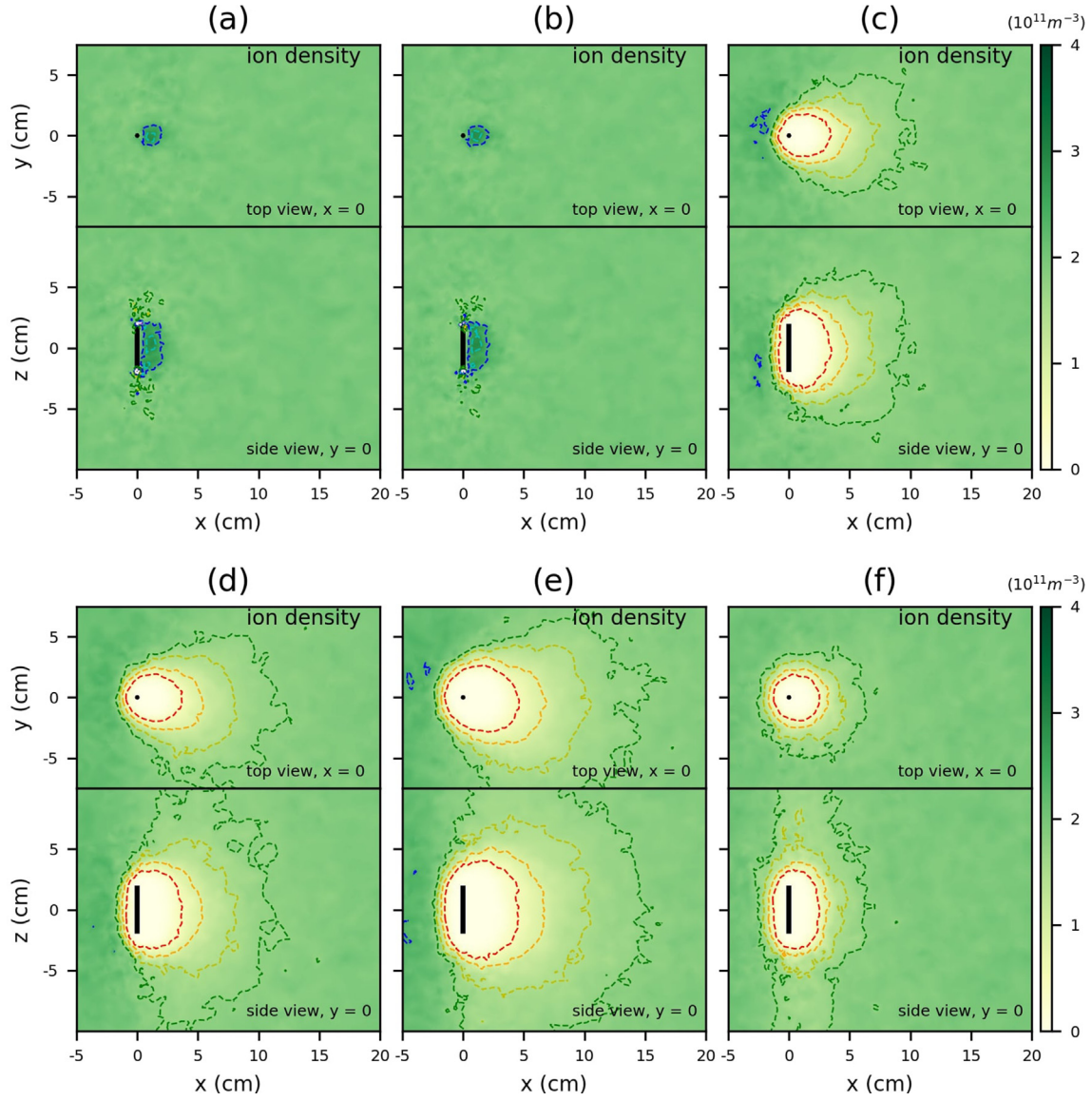

Fig. 3. The top-view (x = 0) and side-view slides (y = 0) of ion density for (a) Case A, (b) Case B, (c) Case C, (d) Case D, (e) Case E, and (f) Case F. The dashed curves show the density contours of 0.5×10^{11} m^{-3} (red curves), 1.0×10^{11} m^{-3} (orange curves), 1.5×10^{11} m^{-3} (yellow curves), 1.75×10^{11} m^{-3} (green curves), 2.4×10^{11} m^{-3} (blue curves), 2.8×10^{11} m^{-3} (cyan curves), 3.2×10^{11} m^{-3} (magenta curves), and 3.6×10^{11} m^{-3} (white curves). The black shadows at the origin of the coordinate system are the placed Langmuir probes. (For interpretation of the references to color in this figure legend, the reader is referred to the web version of this article.)

The m-NLP system generally operates with a positive potential bias. In Case C, we use the same parameters as in Case A but with a fixed 3 V bias applied to the probe. In the electric potential (Fig. 2(c)), we observe a clear potential wake structure in the downstream region of the positive-bias Langmuir probe. As indicated, the potential structure formed is the decaying potential in the probes' closest vicinity following by a negatively charged wake with a minimum potential < -0.06 V (yellow dashed contour). It is a typical wake structure behind a Deybe-scale positively-charged object (Engwall et al., 2006; Miloch et al., 2010; Yaroshenko et al., 2011). As for the density profiles (Fig. 3(c) and Fig. 4(c)), in contrast with Case A, the probes with a positive potential of 3 V will repel ions and collect electrons in the its vicinity. The ion density will go down to 0 in the closest vicinity of the probes (< 2.5 cm, $\sim 3.6\lambda_D$) and slowly increase to the background value. As for the electron density, we find the high-density area in the closest vicinity of the probes and also a low-density groove after $x > 2.5$ cm. The formed wake has a minimum density of $\sim 1.0 \times 10^{11}$ m^{-3} (0.5 n_0, orange dashed contour in Fig. 4)) and extends to $>$ 10cm ($\sim 14.5\lambda_D$).

We have to consider the effects of the magnetic field for Earth's ionosphere applications where the electron gyroradius (1.98 cm) is comparable with our system's spatial scale. With the same parameters as in Case C, here we further apply an external background magnetic field

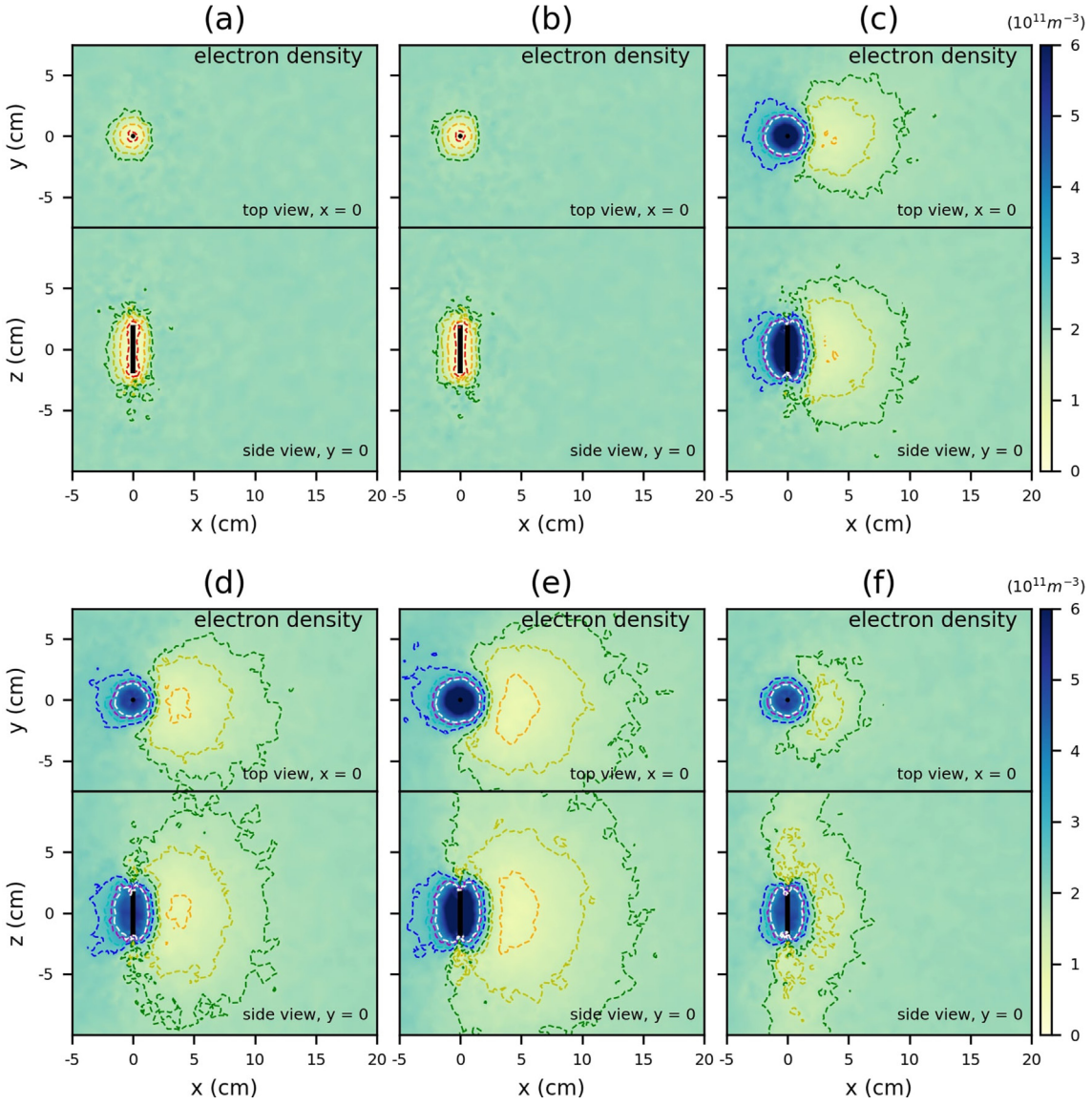

Fig. 4. The top-view (x = 0) and side-view slides (y = 0) of electron density for (a) Case A, (b) Case B, (c) Case C, (d) Case D, (e) Case E, and (f) Case F. The dashed curves show the density contours of $0.5 \times 10^{11} m^{-3}$ (red curves), 1.0×10^{11} m^{-3} (orange curves), 1.5×10^{11} m^{-3} (yellow curves), 1.75×10^{11} m^{-3} (green curves), 2.4×10^{11} m^{-3} (blue curves), 2.8×10^{11} m^{-3} (cyan curves), 3.2×10^{11} m^{-3} (magenta curves), and 3.6×10^{11} m^{-3} (white curves). The black shadows at the origin of the coordinate system are the placed Langmuir probes. (For interpretation of the references to color in this figure legend, the reader is referred to the web version of this article.)

$B_0 = 50$ μT parallel to the probe's axis in Case D. Fig. 2(d), Fig. 3(d), and Fig. 4(d) show respectively the electric potential and density profiles of Case D in the equilibrium. As indicated, the simulation results show a more pronounced plasma wake in Case D's potential and density (magnetized system) than in Case C (unmagnetized system). In particular, we find a clear regime with the electron density is lower than 1.0×10^{11} m^{-3}, that is lower than $0.5n_0$ (orange dashed contour) in Fig. 4(d). However, the positive bias probe will collect fewer electrons in its closest vicinity with the background magnetic field's presence. Previous numerical studies have shown that the background magnetic field's presence will lead to an asymmetric wake structure in the rocket's downstream region (Darian et al., 2017; Usui et al., 2019). With a background magnetic field in the $\hat{z}$ direction, we also find the asymmetric plasma wake in our simulation. For the electric potential profiles, we see the potential wake shifting to the $+\hat{y}$ direction from the top view (top panel) in Case D (Fig. 2(d)) compared with Case C (Fig. 2(c)). As for the electron density profiles, we also find the density wake shifting to the -$\hat{y}$ direction in the magnetized system by comparing Case D (Fig. 3)) and Case C (Fig. 3(c)).

To further investigate the effect of bias on the wake formation, in Case E we increase the fixed bias to 6 V in order to compare the results with Case B (no fixed bias) and Case D (3 V). Fig. 2(e), Fig. 3(e), and Fig. 4(e) show the electric potential and density profiles of Case E in the equilibrium,

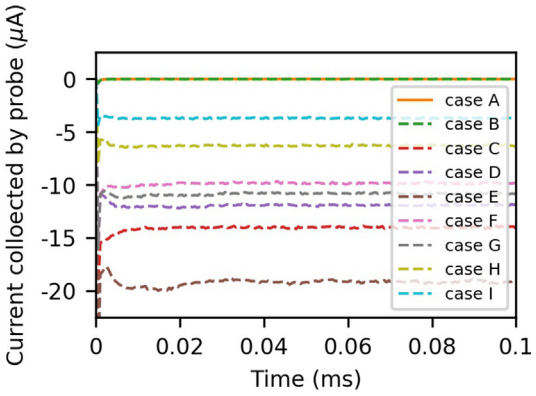

Fig. 5. Evolution of the current collected by probes in all cases. (For interpretation of the references to color in this figure legend, the reader is referred to the web version of this article.)

and Fig. 6 shows the 1D electric potential, ion density, and electron density profiles along the x-axis for Cases B, D, and E. We find that the probe's higher electric bias will enhance the plasma wakes' potential and density perturbations. In particular, we find the minimum potential at < -0.12 V (orange dashed contour) in the plasma wake. Meanwhile, we also find a shift in the density wake as in Case D due to the magnetic field effects. As for the collected current in the equilibrium (Fig. 5), it is higher for the probe with higher bias as expected (Bekkeng et al., 2010; Jacobsen et al., 2010).

Since the relative velocity between the spacecraft and plasma is not always supersonic, we performed additional simulations using the same parameters as in Case D but with a subsonic flow (M = 0.67). This is referred to as Case F. In its steady-state potential profile (Fig. 2(f), the negatively charged potential wake in the downstream region of the probe becomes weaker with the slower plasma flow; particularly, with a minimum potential ~ -0.03 V (blue dashed contour). And, as shown in Fig. 5, the collected current by probe in the equilibrium becomes smaller if the plasma flow is slower (Whipple, 1981). Fig. 7 shows the 1D electric potential, ion density, and electron density profiles along the x-axis for Cases D, F, and G. As indicated (also shown in Fig. 3f) and Fig. 4(f)). The positive-bias Langmuir probe can still repel all ions in its closest vicinity (< 2 cm, $\sim 2.9\lambda_D$). We find a weaker density wake with a minimum density of 1.5×10^{11} m^{-3} (0.75 n_0, yellow dashed contour) extending to $\sim$10 cm ($15\lambda_D$) behind the probe. Note that in Fig. 3f) and Fig. 4(f), we also find the disturbance in both electron density and ion density from the side view along the background magnetic field (also the axis of the probes). Even if we extend the simulation domain in $\pm\hat{z}$ along the probes' axis to 150 Debye lengths, the density disturbances will still exist and persist to the simulation

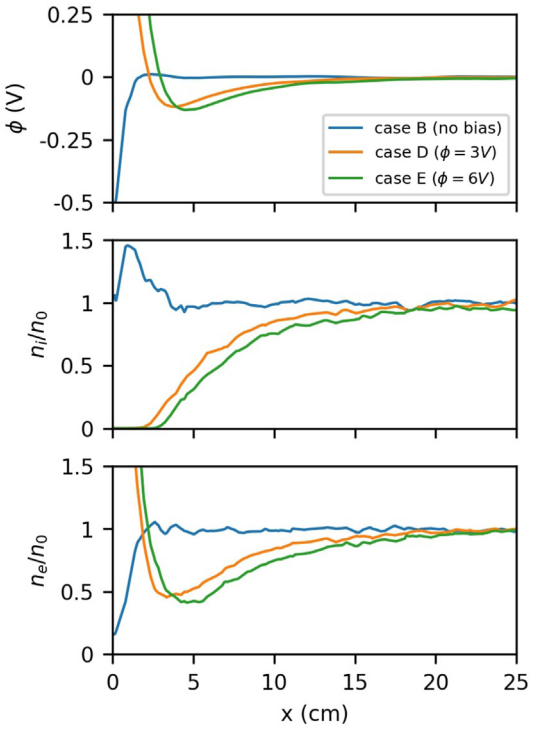

Fig. 6. The electric potential (top panel), electron density (middle panel), and ion density profiles (bottom panel) along the x-axis (y = 0, z = 0) for Case B (no bias, blue curves), Case D ($\phi = 3$ V, orange curves), and Case E ($\phi = 6$ V, green curves). (For interpretation of the references to color in this figure legend, the reader is referred to the web version of this article.)

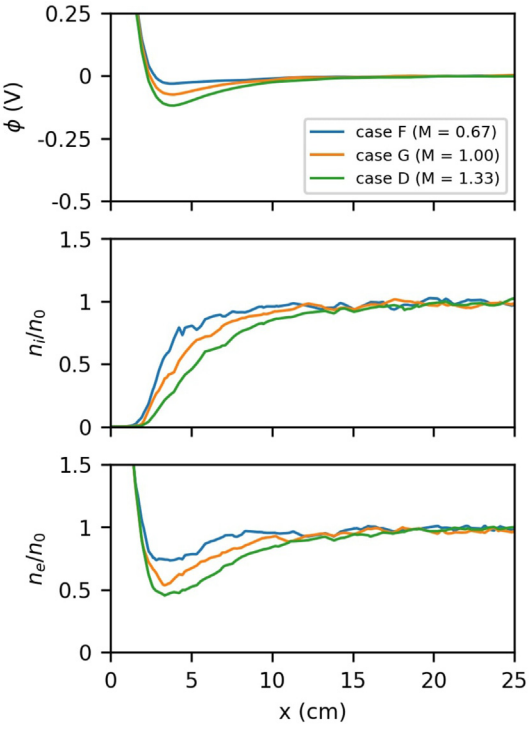

Fig. 7. The electric potential (top panel), electron density (middle panel), and ion density profiles (bottom panel) along the x-axis (y = 0, z = 0) for Case F (M = 0.67, blue curves), Case G (M = 1.00, orange curves), and Case D (M = 1.33, green curves). (For interpretation of the references to color in this figure legend, the reader is referred to the web version of this article.)

domain's boundary. The present wing-like structures are a few electron gyroradii width, and the disturbance regime of ions is downstream of the electron disturbance regime. Similar wing-like structures have been reported around negatively charged spacecraft, where the spacecraft size is larger than an average electron gyroradius of the environment (Miyake et al., 2020). Moreover, the wing-like structures presented in this previous study are with a density higher than the background value. On the other hand, we have a Debye-scale object with positive potential and wing-like structures with a density lower than the background value. The formed wing structures are more pronounced in the subsonic flow case than in the supersonic case.

The last factor we discuss in this paper is the size of the probe. Fig. 8 shows the 1D profile in the downstream region of the object for Case D ($W_P = 4$), Case H ($W_P = 2$), and Case I ($W_P = 1$). With the same 3 V bias applied to the probe, both the ion and electron density recovers earlier for the thinner probe. Fig. 5 also shows that the collected current in the equilibrium is proportional to the probe's diameter, so does the side surface area of the probes (Bekkeng et al., 2010; Jacobsen et al., 2010). However, the electron density wakes all extend to 20 cm ($\sim 30.0\lambda_D$). The simulation results show similar features in the downstream plasma wake as long as the probe is small compared to the Debye length. Note that in the m-NLP instrument, the probe's radius can be smaller than 1 mm. However, considering the computational limitation, we can take the cases with $W_P = 4$ as representative for thinner probes.

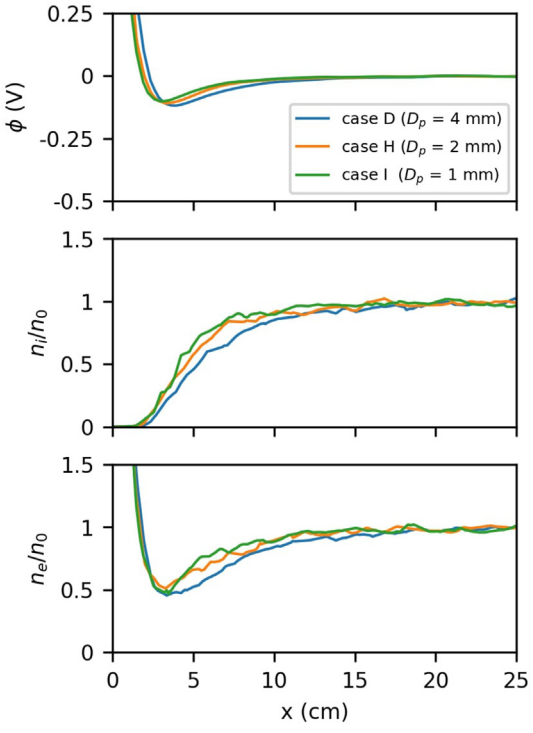

Fig. 8. The electric potential (top panel), electron density (middle panel), and ion density profiles (bottom panel) along the x-axis (y = 0, z = 0) for the Case D ($D_P = 4$ mm, blue curves), Case H ($D_P = 2$ mm, orange curves), Case I ($D_P = 1$ mm, green curves). (For interpretation of the references to color in this figure legend, the reader is referred to the web version of this article.)

In the above paragraphs we have presented the characteristics of the plasma wake under different circumstances based on nine simulation cases. For the in-situ measurement applications, we have carried out a comprehensive survey of the parameter regimes based on 32 simulation cases in the magnetized system ($B_0 = 50$ μT). Fig. 9 shows the 1D potential, ion density, and electron density profiles downstream of a probe with $D_P = 4$ mm for different biases and Mach numbers. As indicated, the Mach number plays a more crucial role in determining the wake's length as compared to the bias effects and the electron density perturbation can extend from 10 cm ($\sim 15.0\lambda_D$) to 20 cm ($\sim 30.0\lambda_D$) for increasing Mach number from 0.7 to 1.3. In addition, the composition of the ionospheric plasma can change significantly with the altitude; specifically, the majority of ions will transfer from oxygen ions to protons from the height above 400 km to 1000 km (Kelley, 1989; Schunk and Nagy, 2009). For the application in the sounding rocket and low Earth orbit satellite missions, here we adopt pure protons (solid curves) and pure oxygen ions (dashed curves), respectively, as the ion component in the background plasma. Compared with the effects of Mach number, the simulation results show that the different ion components do not change the characteristic wake length significantly. This is to be expected, since physical relations between dimension-full quantities (density, drift velocity, etc.), can always be reduced to relations between dimensionless quantities such as the characteristic wake length divided by the Debye length, or, in this case, the Mach number (Buckingham, 1914). For the data processing and the future design of the Langmuir probe instrument, the potential measurement errors can be avoided by referring to these density profiles.

4. Discussion

Previous numerical studies have presented the wake formation problems for positively charged and Debye-scale objects (Engwall et al., 2006; Miloch et al., 2008; Miloch et al., 2010; Yaroshenko et al., 2011). For instance, for the Cluster mission (Engwall et al., 2006), the spacecraft is highly positively charged (20–40 V) while it is traveling in the tenuous plasma (~0.1 cm or less). Moreover, the size of spacecraft (~1.5 m) and boom (~ 80 m) is of the same order as the Debye length in the Earth's magnetospheric plasma (~20 m). When $k_b T_i < m_i u^2/2 < e\phi$ (where ϕ is the potential on the Cluster and the fixed bias on the probe, respectively), the positive potential will scatter the ions and cause a so-called enhanced wake (Engwall et al., 2006). Evidence of such enhanced potential wake was presented in simulations by comparing data from the Electric field and

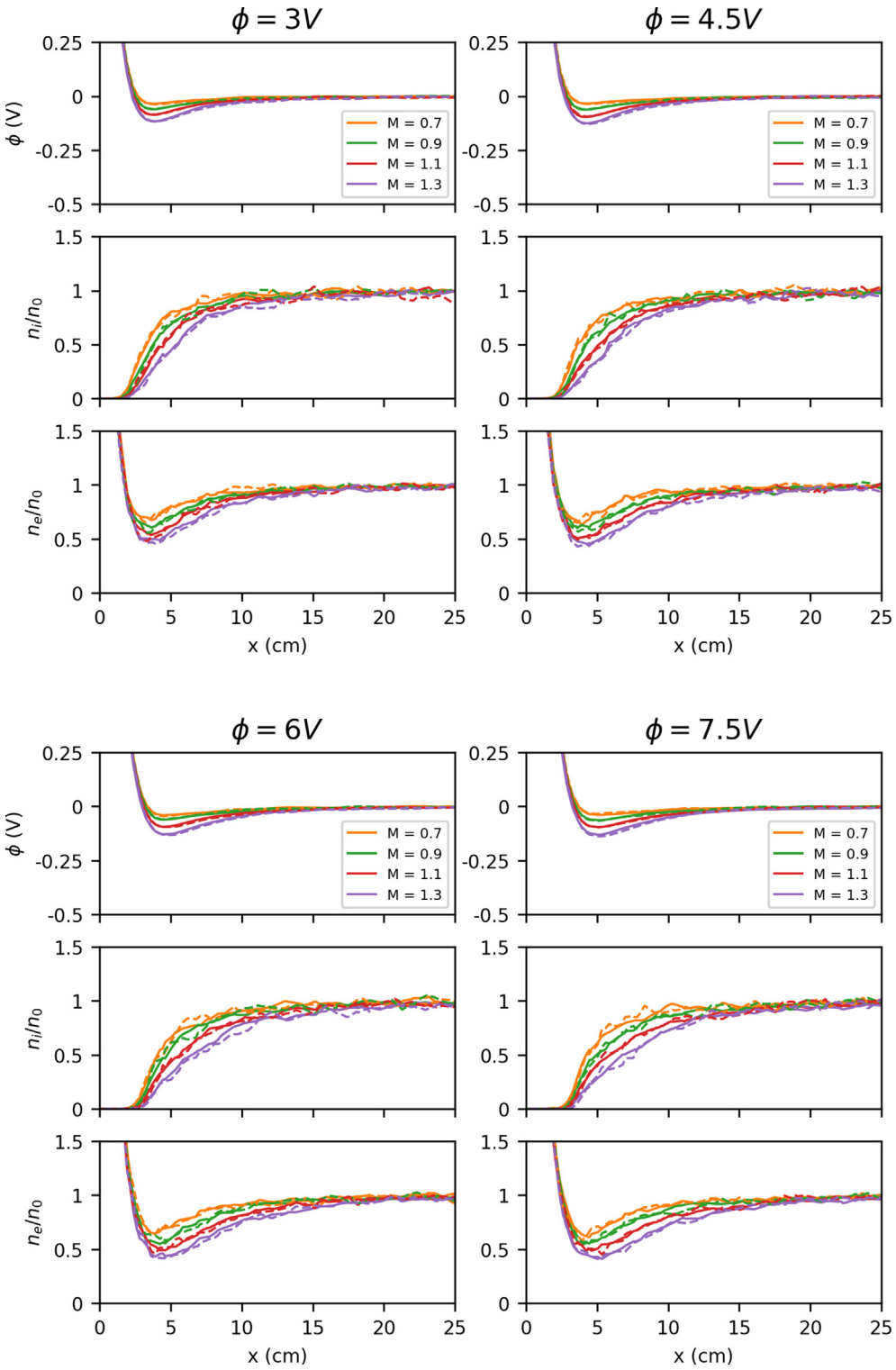

Fig. 9. The electric potential (top panel), electron density (middle panel), and ion density profiles (bottom panel) along the x-axis (y = 0, z = 0) for varied bias (ϕ = 3, 4.5, 6, 7.5 V) and M = 0.7 (orange curves), 0.9 (green curves), 1.1 (red curves), and 1.3 (purple curves). The solid and dashed curves are for the cases adopting protons and oxygen ions, respectively, as the background ions. (For interpretation of the references to color in this figure legend, the reader is referred to the web version of this article.)

Wave instrument (EFW) and the Electron Drift Instrument (EDI) on-board Cluster. As also shown in our simulations, behind the positively charged object, the electric potential decays in the object's closest vicinity, and a negatively charged wake is formed after a few Debye lengths. Even we do not discuss temperature effects in this paper; in their simulation, it shows that the wake's size will decrease with increasing ion temperature and decreasing electron temper-

ature (Engwall et al., 2006). Note that the magnetic field effects are negligible in that previous study because the Larmor radii (several km for ions and a few tens of meters for electrons) are much larger than the spacecraft's and boom's size (Engwall et al., 2006).

For the Cassini mission, similar to our conditions, another study also addresses the wake formation problems during its Saturn orbit insertion flyby. (Yaroshenko et al., 2011). In particular, outside Rhea's dipole shell, the Cassini is positively charged and with a size much smaller than the local plasma's Debye length (0.14 λ_D). This previous study shows both the narrow wake and the enhanced wake by changing the ion temperature. On the other hand, while the spacecraft is in Rhea's shell's direct vicinity, the Cassini's size compared with the local plasma's Debye length is 0.35 λ_D, and the spacecraft will become negatively charged. As presented in Case A in this paper, the simulation results show the ion focusing area behind the relatively small object (Miloch et al., 2008). However, for the application to the Cassini mission, the magnetic field effect is not considered in the simulation either, since the particles' Larmor radii ($>$ 700 m for cold electrons) are much larger than the wake's dimensions (Yaroshenko et al., 2011).

In our study, for focus on wake formation behind Debye-scale Langmuir probes in the F region ionosphere. We find, with a few volts potential bias on the Langmuir probes (3 to 6 V) in a plasma flow with M = 1.33, the plasma wakes in density and electric potential in the downstream region can extend up to 15 Debye lengths ($\sim$ 10.4 cm, according to the parameters used in this paper). As expected, the higher flow velocity enhances the plasma wake's disturbance. However, even in the subsonic case (M = 0.67, Case F), the density wake still extends to $\sim$10 cm (15λ_D) behind the probe. While the m-NLP instrument consists of two or more Debye-scale Langmuir probes, this study gives a necessary distance between the cylindrical probes mounted close to each other. The probe's positive bias is critical for the wake formation behind the Debye-scale object; the higher electric bias can lead to a more pronounced plasma wake behind the Langmuir probe. When there is no fixed bias on the probe (Case A and Case B), the simulation results show the lack of geometric wake due to its tiny size compared with other larger objects (e.g., main rocket body or boom). However, as mentioned above, we can still find the ion focusing area resulting from the negatively charged probe. Note that, since the ion dynamics mainly determines the formation of ion focusing area (Miloch et al., 2008), in Case A and Case B, we do not observe the magnetic field effect due to the relatively large ion gyroradius in our system.

The magnetic field effect plays a significant role in our system, where the electron dynamics determine the mechanism of wake formation. Notably, when we apply a background magnetic field in the simulation, the electron gyroradius (1.98 cm) is of the same order as the wake structure's spatial length. With an external magnetic field along the probes' axis, the plasma wake becomes asymmetric in the electric potential and densities (Darian et al., 2017; Usui et al., 2019). The simulation results also show that the positively charged probe attracts more electrons in its closest vicinity ($< 2\,\lambda_D$) for the unmagnetized case (Case C) compared with the magnetized (Case D). However, the size of the potential and density wakes is larger for the magnetized case.

Furthermore, the simulation results also show the electron density and ion density perturbations along the background magnetic field (also the probe's axis) as a wing-like structure in the magnetized case with a subsonic plasma flow (Case F, M = 0.66). The wing structures are in width of a few electron gyroradii in both electron and ion density profiles. A previous study has reported similar flied-aligned wing structures around the negatively charged spacecraft in the supersonic plasma flow (M = 1.65) (Miyake et al., 2020). Specifically, the reflected electrons from the negatively charged spacecraft will travel out along the background magnetic field. The size of the conductive object (satellite, 0.5 to 2 m) is in the order of the ion's gyroradius (1.5 m). However, in our case, the conductive object (Langmuir probe) has a size $<$ 1 cm, which is in the same order as the electron's gyroradius (1.98 cm). As a result, the present wing-like structures have a width of a few electron gyroradii. Also, note that the wing-like structures are more pronounced in a slower case (Case D, the subsonic case).

5. Summary

In this paper we have studied the wake formation problems in the interaction between positively biased Debye-scale Langmuir probe and its surrounding plasma by employing a three-dimensional unstructured Particle-in-cell code. The choices of the positively biased and Debye-scale Langmuir probe, are set based on the basic concept of the m-NLP instrument which consists of a few thin (smaller than the Debye length) cylindrical probes at different fixed biases and the electron density can be obtained rapidly without operating the classical bias-voltage sweeping (Jacobsen et al., 2010).

We first systematically present the characteristics of the plasma wake under different circumstances. We find that both the higher electric bias and the higher flow velocity can enhance the plasma, and an external magnetic field will also enhance and skew the wake behind a thin cylindrical Langmuir probe. While employing the background magnetic field in the simulation system, we can also observe the wing structures in the density profiles along the background magnetic field. Moreover, based on the 32 simulation cases with a comprehensive survey of practical parameter regimes, we found that the distance between different probes should be at least $15 - 30\lambda_D$ to avoid plasma measurement errors. The adoption of protons or oxygen ions do not change the length of the plasma wake significantly, for similar Mach numbers.

For comparisons with the space mission data, in the future study more factors such as varying plasma densities,

temperatures, flow velocities, and the magnetic field's directions and strengths, should be considered. Additionally, to set up the whole m-NLP instrument and the main spacecraft as well as the boom in the simulation system will be of more practical use for the in-situ missions such as sounding rockets and low Earth orbit satellites. The present study has provided a comprehensive reference for the practical design of such instruments that will limit the wake effects. It is worth noting that this study is not only relevant for the m-NLP technique. For the other instruments (e.g., the electric field probes thinner than the Debye Length) placed on the boom but far away from the payload body, the plasma wake formed behind one probe can also cause the measurement error on other instruments.

Declaration of Competing Interest

The authors declare that they have no known competing financial interests or personal relationships that could have appeared to influence the work reported in this paper.

Acknowledgments

The authors thank Richard Marchand for permission to use PTetra. C.-S. Jao acknowledges the support of Ministry of Science and Technology (109-2811-M-008-539 and 109-2111-M-008-027-MY2) and National Center for High-performance Computing (NCHC) of National Applied Research Laboratories (NARLabs) in Taiwan for providing computational and storage resources. The work is also supported by the European Research Council (ERC) under the European Union's Horizon 2020 research and innovation programme (ERC Consolidator Grant agreement No. 866357, POLAR-4DSpace) and by the Research Council of Norway grant 275653. S. Marholm gratefully acknowledges Dag Mortensen and the Institute for Energy Technology for being allowed to participate in this research. The simulations were also performed on resources provided by UNINETT Sigma2 - the National Infrastructure for High Performance Computing and Data Storage in Norway (Notur project nn9299k).

References

Al'pert, Y.L., Gurevich, A.V., Pitaevskii, L.P., 1966. Space physics with artificial satellites. Am. J. Phys. 34 (6), 544–544.

Antonsen, T., Havnes, O., Spicher, A., 2019. Multi-scale measurements of mesospheric aerosols and electrons during the maxidusty campaign. Atmos. Meas. Tech. 12 (4), 2139–2153.

Bekkeng, T.A., Barjatya, A., Hoppe, U.-P., Pedersen, A., Moen, J.I., Friedrich, M., Rapp, M., 2013. Payload charging events in the mesosphere and their impact on langmuir type electric probes. Ann. Geophys. 31 (2), 187–196.

Bekkeng, T.A., Jacobsen, K.S., Bekkeng, J.K., Pedersen, A., Lindem, T., Lebreton, J.-P., Moen, J.I., 2010. Design of a multi-needle langmuir probe system. Meas. Sci. Technol. 21 (8), 085903.

Buckingham, E., 1914. On physically similar systems; illustrations of the use of dimensional equations. Phys. Rev. 4 (4).

Chernyshov, A.A., Chugunin, D.V., Frolov, V.L., Clausen, L.B.N., Miloch, W.J., Mogilevsky, M.M., 2020. In situ observations of ionospheric heating effects: First results from a joint sura and norsat-1 experiment. Geophys. Res. Lett. 47 (13), e2020GL088462.

Darian, D., Marholm, S., Paulsson, J.J.P., Miyake, Y., Usui, H., Mortensen, M., Miloch, W.J., 2017. Numerical simulations of a sounding rocket in ionospheric plasma: Effects of magnetic field on the wake formation and rocket potential. J. Geophys. Res. Space Phys. 122 (9), 9603–9621.

Deca, J., Lapenta, G., Marchand, R., Markidis, S., 2013. Spacecraft charging analysis with the implicit particle-in-cell code ipic3d. Phys. Plasmas 20 (10), 102902.

Endo, K., Kumamoto, A., Katoh, Y., 2015. Observation of wake-induced plasma waves around an ionospheric sounding rocket. J. Geophys. Res. Space Phys. 120 (6), 5160–5175.

Engwall, E., Eriksson, A.I., Forest, J., 2006. Wake formation behind positively charged spacecraft in flowing tenuous plasmas. Phys. Plasmas 13 (6), 062904.

Eriksson, A.I., André, M., Klecker, B., Laakso, H., Lindqvist, P.-A., Mozer, F., Paschmann, G., Pedersen, A., Quinn, J., Torbert, R., Torkar, K., Vaith, H., 2006. Electric field measurements on cluster: comparing the double-probe and electron drift techniques. Ann. Geophys. 24 (1), 275–289.

Fowler, C.M., Andersson, L., Ergun, R.E., Morooka, M., Delory, G., Andrews, D.J., Lillis, R.J., McEnulty, T., Weber, T.D., Chamandy, T. M., Eriksson, A.I., Mitchell, D.L., Mazelle, C., Jakosky, B.M., 2015. The first in situ electron temperature and density measurements of the martian nightside ionosphere. Geophys. Res. Lett. 42 (21), 8854–8861.

Gurevich, A.V., Pitaevskii, L.P., Smirnova, V.V., 1969. Ionospheric aerodynamics. Space Sci. Rev. 9 (6), 805–871.

Hastings, D.E., 1995. A review of plasma interactions with spacecraft in low earth orbit. J. Geophys. Res. Space Phys. 100 (A8), 14457–14483.

Hoang, H., Clausen, L.B.N., Røed, K., Bekkeng, T.A., Trondsen, E., Lybekk, B., Strøm, H., Bang-Hauge, D.M., Pedersen, A., Spicher, A., Moen, J.I., 2018. The multi-needle langmuir probe system on board norsat-1. Space Sci. Rev. 214 (4), 75.

Hoang, H., Røed, K., Bekkeng, T.A., Moen, J.I., Clausen, L.B.N., Trondsen, E., Lybekk, B., Strøm, H., Bang-Hauge, D.M., Pedersen, A., Nokes, C.D.A., Cupido, C., Mann, I.R., Ariel, M., Portnoy, D., Sagi, E., 2019. The multi-needle langmuir probe instrument for qb50 mission: Case studies of ex-alta 1 and hoopoe satellites. Space Sci. Rev. 215 (2), 21.

Howard, L.N., 1961. Note on a paper of john w. miles. J. Fluid Mech. 10 (4), 509–512.

Hutchinson, I.H., 2012. Electron velocity distribution instability in magnetized plasma wakes and artificial electron mass. J. Geophys. Res. Space Phys. 117 (A3).

Jacobsen, K.S., Pedersen, A., Moen, J.I., Bekkeng, T.A., 2010. A new langmuir probe concept for rapid sampling of space plasma electron density. Meas. Sci. Technol. 21 (8), 085902.

Kelley, M.C., 1989. Chapter 2 - fundamentals of ionospheric plasma dynamics. In: Kelley, M.C. (Ed.), The Earth's Ionosphere. Academic Press, pp. 23–63.

Liu, V.C., 1969. Ionospheric gas dynamics of satellites and diagnostic probes. Space Sci. Rev. 9 (4), 423–490.

Marchand, R., 2012. Ptetra, a tool to simulate low orbit satellite–plasma interaction. IEEE Trans. Plasma Sci. 40 (2), 217–229.

Marchand, R., Resendiz Lira, P.A., 2017. Kinetic simulation of spacecraft–environment interaction. IEEE Trans. Plasma Sci. 45 (4), 535–554.

Marholm, S., Marchand, R., 2020. Finite-length effects on cylindrical langmuir probes. Phys. Rev. Res. 2, 023016.

Marholm, S., Marchand, R., Darian, D., Miloch, W.J., Mortensen, M., 2019. Impact of miniaturized fixed-bias multineedle langmuir probes on cubesats. IEEE Trans. Plasma Sci. 47 (8), 3658–3666.

Miloch, W.J., Rekaa, V.L., Pecseli, H.L., Trulsen, J., 2010. Ion acoustic double layers forming behind irradiated solid objects in streaming plasmas. J. Plasma Phys. 76 (3–4), 429–439.

Miloch, W.J., Trulsen, J., Pécseli, H.L., 2008. Numerical studies of ion focusing behind macroscopic obstacles in a supersonic plasma flow. Phys. Rev. E 77, 056408.

Miloch, W.J., Vladimirov, S.V., Pécseli, H.L., Trulsen, J., 2008. Wake behind dust grains in flowing plasmas with a directed photon flux. Phys. Rev. E 77, 065401.

Miyake, Y., Cully, C.M., Usui, H., Nakashima, H., 2013. Plasma particle simulations of wake formation behind a spacecraft with thin wire booms. J. Geophys. Res. Space Phys. 118 (9), 5681–5694.

Miyake, Y., Miloch, W.J., Kjus, S.H., Pcseli, H.L., 2020. Electron wing-like structures formed at a negatively charged spacecraft moving in a magnetized plasma. J. Geophys. Res. Space Phys. 125 (2), e2019JA027379.

Moen, J., Oksavik, Kjellmar, Alfonsi, Lucilla, Daabakk, Yvonne, Romano, Vineenzo, Spogli, Luca, 2013. Space weather challenges of the polar cap ionosphere. J. Space Weather Space Clim. 3, A02.

Moen, J., Spicher, A., Rowland D.E., Kletzing, C., LaBelle, J., 2018. Grand challenge initiative–cusp: rockets to explore solar wind-driven dynamics of top side polar atmosphere. In: SESS 2018 The State of Environmental Science in Svalbard. Svalbard Integrated Arctic Earth Observing System, Longyearbyen, pp. 184– 204.

Mott-Smith, H.M., Langmuir, I., 1926. The theory of collectors in gaseous discharges. Phys. Rev. 28, 727–763.

Paulsson, J.J.P., Miyake, Y., Miloch, W.J., Usui, H., 2019. Effects of booms of sounding rockets in flowing plasmas. Phys. Plasmas 26 (3), 032902.

Paulsson, J.J.P., Spicher, A., Clausen, L.B.N., Moen, J.I., Miloch, W.J., 2018. Wake potential and wake effects on the ionospheric plasma density measurements with sounding rockets. J. Geophys. Res. Space Phys. 123 (11), 9711–9725.

Roussel, J.-F., Berthelier, J.-J., 2004. A study of the electrical charging of the rosetta orbiter: 1. Numerical model. J. Geophys. Res. Space Phys. 109 (A1).

Rylina, I.V., Zynin, L.V., Grigoriev, S.A., Veselov, M.V., 2002. Hydrodynamic approach to modeling the thermal plasma distribution around a moving charged satellite. Cosm. Res. 40 (4), 367–377.

Samir, U., Wright Jr., K.H., Stone, N.H., 1983. The expansion of a plasma into a vacuum: Basic phenomena and processes and applications to space plasma physics. Rev. Geophys. 21 (7), 1631–1646.

Schunk, R., Nagy, A., 2009. Ionospheres: Physics, Plasma Physics, and Chemistry. Cambridge Atmospheric and Space Science Series, second ed. Cambridge University Press.

Shebanits, O., Hadid, L.Z., Cao, H., Morooka, M.W., Hunt, G.J., Dougherty, M.K., Wahlund, J.-E., Waite, J.H., Müller-Wodarg, I., 2020. Saturn's near-equatorial ionospheric conductivities from in situ measurements. Sci. Rep. 10 (1), 7932.

Spicher, A., Ilyasov, A.A., Miloch, W.J., Chernyshov, A.A., Clausen, L.B. N., Moen, J.I., Abe, T., Saito, Y., 2016. Reverse flow events and small-scale effects in the cusp ionosphere. J. Geophys. Res. Space Phys. 121 (10), 10466–10480.

Toledo-Redondo, S., Lavraud, B., Fuselier, S.A., Andr, M., Khotyaintsev, Y.V., Nakamura, R., Escoubet, C.P., Li, W.Y., Torkar, K., Cipriani, F., Barrie, A.C., Giles, B., Moore, T.E., Gershman, D., Lindqvist, P.-A., Ergun, R.E., Russell, C.T., Burch, J.L., 2019. Electrostatic spacecraft potential structure and wake formation effects for characterization of cold ion beams in the earth's magnetosphere. J. Geophys. Res. Space Phys. 124(12), 10048–10062.

Usui, H., Miyake, Y., Miloch, W.J., Ito, K., 2019. Numerical study of plasma depletion region in a satellite wake. IEEE Trans. Plasma Sci. 47 (8), 3717–3723.

Wang, J., Hastings, D.E., 1992. Ionospheric plasma flow over large high?? oltage space platforms. ii: The formation and structure of plasma wake. Physics of Fluids B. Plasma Phys. 4 (6), 1615–1629.

Whipple, E.C., 1981. Potentials of surfaces in space. Rep. Prog. Phys. 44 (11), 1197–1250.

Yaroshenko, V.V., Miloch, W.J., Vladimirov, S., Thomas, H.M., Morfill, G.E., 2011. Modeling of cassini's charging at saturn orbit insertion flyby. J. Geophys. Res. Space Phys. 116 (A12).